

Mechanical metal-insulator transition in 2D graphene phononic crystals

Jan N. Kirchhof^{d} and Kirill I. Bolotin^{l*}*

^l Department of Physics, Freie Universität Berlin, Arnimallee 14, 14195 Berlin, Germany

[*jan.kirchhof@fu-berlin.de](mailto:jan.kirchhof@fu-berlin.de) [*kirill.bolotin@fu-berlin.de](mailto:kirill.bolotin@fu-berlin.de)

We present of a tunable phononic crystal which undergoes a phase transition from mechanically insulating to mechanically transmissive (metallic). Specifically, in our simulations for a phononic lattice under biaxial tension ($\sigma_{xx} = \sigma_{yy} = 0.01$ N/m), we find a bandgap in the range of 48.8 – 56.4 MHz, which we can close by increasing the degree of tension uniaxiality (σ_{xx}/σ_{yy}) to 1.7. To manipulate the tension distribution, we design a realistic device of finite size, where σ_{xx}/σ_{yy} is tuned by applying a gate voltage to a phononic crystal made from suspended graphene. We show that the phase transition can be probed via acoustic transmission measurements and that the phononic bandgap persists even after the inclusion surface contaminants and random tension variations present in realistic devices. The proposed system acts as a transistor for phonons with an on/off ratio of 10^5 (100 dB suppression) and is thus a valuable extension for phonon logic applications. In addition, this mechanical analogue to a metal-insulator transition (mMIT) allows tunable coupling between mechanical entities (e.g. mechanical qubits).

INTRODUCTION

Phononic crystals (PnCs) are artificial structures in which the periodic variation of material properties (e.g. stiffness, mass, or tension) give rise to a phononic band structure – in analogy to Bloch waves in crystalline solids. In contrast to conventional solids, the parameters of the band structure can be broadly controlled via artificial patterning. Because of that, PnCs allow realizing analogues of fundamental solid state physics phenomena over a very large range of sizes (10 nm – 100 μ m) and frequencies (Hz - THz).^{1,2} This ranges from quantum entanglement^{3,4} to topological states^{5,6} and negative refraction.⁷ The ability to engineer phononic spectra gave rise to applications such as phononic shielding in ultracoherent mechanical resonators,^{8–11} wave guiding^{12,13} or thermal management.¹⁴ Due to the much lower propagation speed of phonons compared to photons or electrons, PnCs are also promising candidates for quantum information technology based on guiding and storing mechanical motion, especially on length scales too small for photonic approaches.^{6,15–18} Most of these applications and phenomena rely on phononic bandgaps, the range of frequencies where no phonons are allowed and mechanical motion is heavily damped.

The velocities of all phonons in a material depend on its tension σ . In conventional rigid PnCs, e.g. those fabricated using silicon nitride membranes (SiN_x), the built-in tension is determined during the growth step and cannot be tuned. As a result, it becomes challenging to couple a PnC to an external system, for example for processing and storing of quantum information.^{19–21} In contrast, it has been recently demonstrated that the tension in much more flexible two-dimensional (2D) materials can be dynamically controlled by applying electrostatic pressure via an external gate electrode.^{22–25} The resulting tunable (biaxial) tension allows broad tunability of the of the bandgap centre frequency.²³ Nevertheless, the topology of the bands in the systems explored so far has not been affected by tension – i.e. a gapped system remained gapped at any tension level. The precise control of the bandgap size and thus the coupling strength between mechanical entities remains elusive.

Here, we show that the application of uniaxial tension (in contrast to biaxial tension studied previously) changes the band topology. Specifically, for a PnC made from suspended graphene under biaxial tension

($\sigma_{xx}/\sigma_{yy} = 1$), we observe a bandgap at any tension (e.g. 48.8 – 56.4 MHz at $\sigma = 0.01$ N/m), which disappears completely when the degree of tension uniaxiality (σ_{xx}/σ_{yy}) reaches 1.7. This constitutes the observation of a mechanical analogue to a metal-insulator transition (mMIT). To control σ_{xx}/σ_{yy} , we propose a simple experimental geometry based on electrostatic gating and show that bandgap closing can be reached in experimentally feasible devices, which we probe via acoustic transmission studies. Our simulations show that applying a small gate voltage of ~ 8 V to the suspended graphene PnC is sufficient to drive the mMIT. The system functions as a mechanical transistor with an on/off ratio of 10^5 (suppression of 100 dB) and can be used in phonon logic circuits. Furthermore, the ability to dynamically control the bandgap size allows to realize tunable coupling strength between mechanical entities e.g. two mechanical resonators acting as qubits. Finally, we investigate the challenges associated with the fabrication of 2D materials. We find that the mass of contaminants on top of the device must be smaller than ~ 4 times the weight of the suspended graphene and that the relative tension variation in the graphene must be smaller than 40% to observe a clear bandgap and the proposed mMIT.

RESULTS

PnC design

For the design of our tunable 2D phononic system we choose a honeycomb lattice (lattice constant a) of holes (diameter d), which provides a relatively broad and robust bandgap while leaving a large fraction of the material untouched. The latter is crucial for making a PnC from fragile 2D materials. The honeycomb lattice also features an indirect phononic bandgap, which allows selective tuning of phononic bands via uniaxial tension, as we will see later. Our material of choice is graphene, the most conductive^{26,27} and the strongest member of the family of 2D materials.²⁸ Our results are also applicable to other conductive 2D materials. We consider a free-standing PnC to allow mechanical tuning via out-of-plane pressure. Fabrication of such devices has recently been demonstrated by He-Ion beam milling.^{23,29,30} To obtain the phononic band structure, we start by performing finite element method (FEM) simulations of the tension distribution within the unit cell of the honeycomb lattice (Fig. 1a, top). We find tension hotspots in the thin ribbons and relaxed regions in the centre of the unit cell. This

redistribution of tension occurs when holes are cut into the initially uniform membrane. In a next step, we use the first Brillouin zone (Fig. 1a, bottom) to calculate the phononic band structure along the high symmetry lines for an infinite lattice, as shown Fig. 1b for $a = 1 \mu\text{m}$, $d/a = 0.5$ and a reasonable initial biaxial tension of $\sigma_{xx} = \sigma_{yy} = 0.01 \text{ N/m}$.^{23,31,32} For out-of-plane modes (solid lines) we find a bandgap between 48.8 and 56.4 MHz (blue shaded), in agreement with previous work.^{23,30} The entire phononic lattice behaves like a thin membrane with vibrational mode frequencies f determined by the built-in tension ($f \sim \sqrt{\sigma}$). Also, in agreement with previous work, we find that an increase in uniform tension ($\sigma_{xx}/\sigma_{yy} = 1$) leads to monotonic upscaling of both the top of valence (f_{VB}) and bottom of conduction band (f_{CB}) frequencies as shown in Fig. 1e (red). Here, the centre frequency of the bandgap follows a square root behaviour vs. tension, and the relative bandgap size $(\frac{f_{CB} - f_{VB}}{(f_{CB} + f_{VB})/2})$ remains constant.

mMIT for highly uniaxial tension

Our next goal is to show that we can use uniaxial tension (unlike biaxial tension) to control the relative bandgap size and even completely close it. The phononic bandgap of a hexagonal lattice is indirect with the conduction band minima f_{CB} , located at the Γ point in momentum space and the valence band maxima f_{VB} , at a point along the ΓX line (Fig. 1b). Critically, uniaxial tension, in contrast to biaxial tension, produces different frequency scaling of the band structure at different points of the Brillouin zone. With increasingly uniaxial tension, f_{VB} strongly upshifts in frequency while f_{CB} is barely tension-dependent. As a result, the indirect bandgap of the phononic lattice acquires a strong tension-dependence. To quantify these changes, we determine the average tension components (after redistribution upon phononic patterning) $\sigma_{ij} = \langle \sigma_{ij} \rangle$ and use the ratio σ_{xx}/σ_{yy} as a metric for tension uniaxiality. For the honeycomb lattice with its initial tension distribution (as introduced above), $\sigma_{xx}/\sigma_{yy} = 1$. For an increased $\sigma_{xx}/\sigma_{yy} = 1.35$, we find increased tension in the areas stretched in the x -direction (Fig. 1c, inset). This is accompanied by a much more pronounced upshift of f_{VB} compared to f_{CB} and thus a reduced bandgap size (Fig. 1c). To give an intuitive understanding of this scaling behaviour, we look at the spatial shape of modes corresponding to f_{VB} and f_{CB} . The mode f_{CB} at the Γ point (Fig. 1b, left inset) resembles a standing wave along the y direction, and it therefore does not

depend strongly on tension in the x direction. The mode corresponding to f_{VB} , between Γ and X (Fig. 1b, right inset), resembles a linear combination of standing waves in the x and y directions. The frequency of this mode however does depend on σ_{xx} . For a higher uniaxiality of 1.7 as shown in Fig. 1d, the tension distribution becomes even more distorted (Fig. 1d inset) and the lower branches (f_{VB}) overtake the upper ones (f_{CB}). At this point, the bandgap closes ($\frac{f_{CB}-f_{VB}}{(f_{CB}+f_{VB})/2} = 0$). In the Supplementary information, we provide extended band structure calculations showing the full extent of the Brillouin zone under uniaxial tension.

To summarize the results of bandgap tuning, in Fig. 1e we compare f_{VB} and f_{CB} vs. the total tension σ_{total} for uniaxial (blue) and uniform biaxial (red) tension. For uniaxial tension, we see a closing of the bandgap at $\sigma_{total}/\sigma_0 = 1.6$ (corresponds to $\sigma_{xx}/\sigma_{yy} = 1.7$). In contrast, for biaxial tension scaling, the bandgap increases in absolute size with increased tension, while the relative bandgap size remains constant. Overall, by varying the tension uniaxiality, we find different scaling behaviour for different phononic bands along different directions, which allows us to dynamically tune the size of the bandgap.

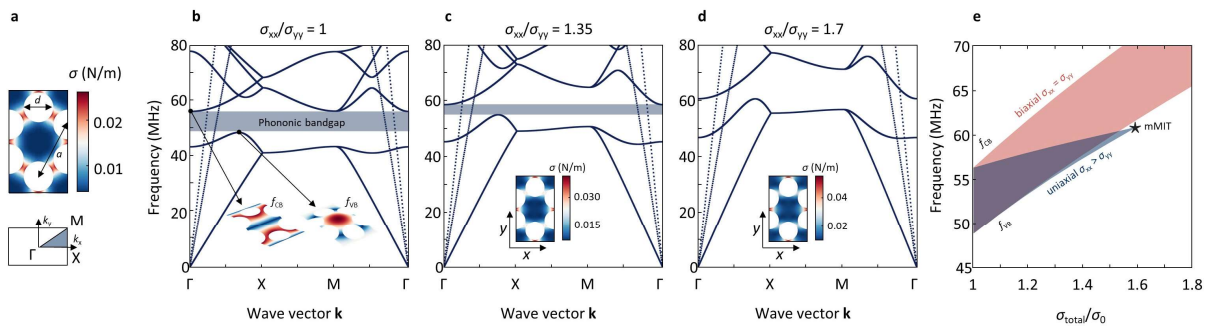


Figure 1 | Mechanical metal-insulator transition induced by uniaxial tension. **a**, Unit cell of the honeycomb lattice with redistributed tension (top) and the corresponding first Brillouin zone (bottom). **b**, Phononic band structure for the unit cell shown in (a) under uniform tension ($\sigma_{xx} = \sigma_{yy} = 0.01$ N/m). For out-of-plane modes (solid lines) a clear phononic bandgap is visible (blue shaded region). The insets show the mode shape (displacement) within the unit cell at the points above and below the bandgap. **c,d**, Phononic band structure and tension distribution in the unit cell (insets) for σ_{xx}/σ_{yy} of 1.35 and 1.7. With increasing uniaxiality in tension ($\sigma_{xx}/\sigma_{yy} > 1$), the phononic bands show different frequency scaling behavior along different high symmetry lines. At $\sigma_{xx}/\sigma_{yy} = 1.7$, the phononic bandgap closes and the system becomes mechanically metallic. **e**, Phononic bandgap for biaxial (red) and uniaxial (blue) tension vs. total normalized tension. When the tension is increased biaxially ($\sigma_{xx} = \sigma_{yy}$), the bandgap centre frequency rises, and the bandgap width increases. On the contrary, uniaxial upscaling ($\sigma_{xx} > \sigma_{yy}$) leads to a bandgap closing.

Our next goal is to develop a design for an experimentally feasible device realizing the mMIT. To accomplish this, three challenges need to be overcome. First, how can we probe the phononic bandgap in a realistic finite-size device? This is critical as the band structure calculations considered so far always assume an infinite phononic lattice. Second, how can we generate the highly uniaxial tension distribution needed to induce the mMIT? Third, is it feasible to fabricate a sufficiently uniform PnC from experimentally available 2D materials? We now individually address each of these questions in the next sections.

Bandgap probing in a finite-size device

We probe our finite-size phononic system via acoustic transmissions measurements. In general, the transmission across a phononic system is determined by the density of available states at the relevant frequency which serves as a proxy for the phononic band structure. We design a transistor-style PnC with realistic dimensions of $9\ \mu\text{m} \times 28\ \mu\text{m}$ (7×17 unit cells, unlike the infinite system considered in simplified simulations so far), in which instead of electrons we will determine the transmission of mechanical motion (Fig. 2a). At point A (excitation/source) mechanical motion is excited, which then can propagate through the PnC until it reaches point B (detection/drain). Drive and detection in such a device design can be experimentally realized by using either surface acoustic waves (SAW),¹⁵ local gate electrodes³³ or two spatially separated laser beams¹² (blue, red Fig. 2a). Here, we concentrate without loss of generality on the last case. We define the transmission from area A to B as:

$$Transmission_{A \Rightarrow B}(f) = \frac{1}{T} \int_0^T \frac{\iint_A z(x,y,f,t) dA}{\iint_B z(x,y,f,t) dA} dt,$$

where $z(x, y, f, t)$ is the out of plane displacement of the suspended graphene with a period T ($f = \frac{1}{T}$).

The integration is over the illumination areas in points A and B. We concentrate on out-of-plane modes as they are controlled by the in-plane phononic pattern, show strong capacitive coupling to perpendicular electric fields from a gate electrode and are sensitive to interferometric readout. In Fig. 2b, we plot the transmission vs. frequency for the device shown in Fig. 2a. In the region below the fundamental resonance, the stop band (< 5 MHz), we find strongly suppressed transmission. Towards

higher frequencies, we find multiple closely spaced sharp peaks, which correspond to higher order resonances of the device. As the frequency increases further, the transmission is more and more dominated by the phononic band structure, and we observe broad “bands” rather than individual resonance modes. The transmission suddenly drops by an average of 5 orders magnitude in the expected bandgap region between 48.5 and 56.5 MHz (blue shaded). The non-zero transmission inside the bandgap is related to finite-size effects captured by our model. Above the bandgap the transmission recovers and remains close to 1. The frequency range of the bandgap extracted from transmission simulations matches well with the bandgap from band structure calculations (comp. Fig. 1b). To summarize, we can use acoustic transmission studies to probe the phononic bandgap in finite-size devices. Furthermore, transmission of mechanical motion across the device in the bandgap region is strongly suppressed and, in analogy to an electronic system, the system can be considered a mechanical insulator.

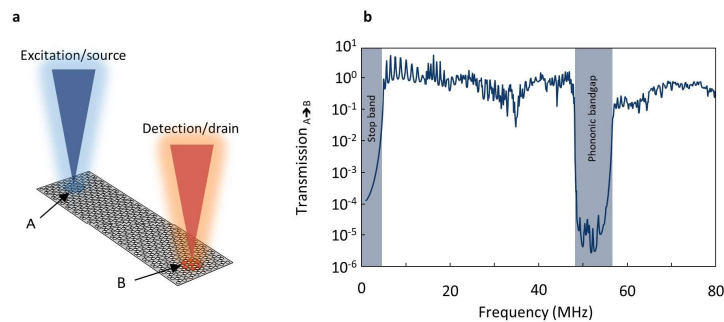


Figure 2 | Probing the band structure via transmission studies in a finite-size phononic crystal. **a**, Transmission geometry for a rectangular phononic device. At point A mechanical motion is excited by a frequency modulated laser (blue). The vibrational wave travels through the device and is detected at point B by a second laser spot (red). **b**, Transmission from A to B vs. excitation frequency for the device shown in (a). A clear bandgap region is visible (blue shaded) where transmission of mechanical motion through the device is suppressed by $\sim 10^5$.

Uniaxial tension engineering

After finding the mMIT in band structure calculations at a tension uniaxiality of $\sigma_{xx}/\sigma_{yy} = 1.7$ and establishing transmission studies as a suitable approach to probe the bandgap, we now aim to produce the required tension distribution – and hence the mMIT – in a realistic device of finite size. Our key idea is to apply electrostatic pressure to a suspended rectangular device (Fig. 3a) with non-unity aspect

ratio (W/L). In this case the induced tension is larger along the direction of the smaller spatial dimension (x in Fig. 3a).³⁴ We model the membrane as clamped at its perimeter. Electrostatic pressure p_{el} is generated by applying a gate voltage (V_{gate}) between the highly conductive graphene and a gate electrode separated from it by distance d :

$$p_{el} = \frac{\epsilon_0}{2} \left(\frac{V_{gate}}{d} \right)^2,$$

where ϵ_0 is the vacuum permittivity. We assume $d = 300$ nm, a typical oxide thickness for Si/SiO₂ substrates used for 2D materials. At zero gate voltage, corresponding to zero pressure, the membrane is uniformly tensed ($\sigma_{xx} \approx \sigma_{yy}$). The tension distribution inside the center of the phononic device is plotted in Fig. 3b. With applied pressure the degree of tension uniaxiality σ_{xx}/σ_{yy} increases and the distribution of tension becomes rotationally asymmetric (Fig. 3c). For $p_{el} = 3$ kPa (8V), σ_{xx}/σ_{yy} reaches 1.7 and we thus expect the mMIT to occur. The generated tension distribution also matches the prediction for the mMIT from our band structure calculations – compare dashed outline in Fig. 3c with the inset of Fig. 1d. In Fig. 3d we summarize the results of tension engineering for our finite-size system in a phase diagram, where we plot σ_{xx}/σ_{yy} vs. applied pressure vs. aspect ratio. When σ_{xx}/σ_{yy} reaches the critical value of 1.7 (dashed line), we expect bandgap closing according to our band structure calculations for the infinite lattice. This line can therefore be viewed as a boundary separating a mechanically insulating from a mechanically metallic (transmissive) phase. We see that the metallic phase is reached at lowest applied pressure for an aspect ratio of $W/L = 0.32$.

Next, we calculate the transmission spectra for applied pressures of 0 and 5 kPa (Fig. 3e). While we find a clear bandgap (and higher order harmonics) for the un-pressured state (blue), the bandgap completely vanishes with applied pressure (red, 5 kPa), confirming the expected mMIT for a finite-size phononic crystal. The system is now transmissive and mechanically metallic. Continuing the analogy between phononic and electronic devices, our system can be viewed as a mechanical transistor with an on/off ratio of $\sim 10^5$ (100 dB suppression).

In Fig. 3f, we show combined results from multiple pressures by plotting f_{VB} and f_{CB} for the rectangular device ($W/L = 0.32$, blue) and a circular reference device (red). In accordance with previous simplified calculations (Fig. 1e), we see that the bandgap $\frac{f_{CB}-f_{VB}}{(f_{CB}+f_{VB})/2}$ gradually decreases in size with applied pressure for the rectangular device. The applied pressure increases σ_{xx}/σ_{yy} and drives the system towards the mMIT. In contrast, the circular reference device for which we expect entirely biaxial tension tuning ($\sigma_{xx} \approx \sigma_{yy}$) exhibits a clear bandgap up to 30 kPa (see Supplementary information). To better relate our results to the phononic band structure calculations, we take the average tension values (σ_{xx} , σ_{yy} and σ_{total}) from the finite-size system under pressure as input for our infinite model and plot the expected bandgap regions in Fig. 3f (red and blue shaded). While we find comparable behaviour, the mMIT however occurs at somewhat higher pressures. This is likely due to boundary-related disorder that is excluded in the infinite model. To summarize, we find bandgap closing for a highly uniaxial tension distribution generated by applying electrostatic pressure in a realistic finite-size device with optimized geometry. This allows us to change the phase of a PnC from mechanically insulating to metallic (transmissive) by simply applying a gate voltage.

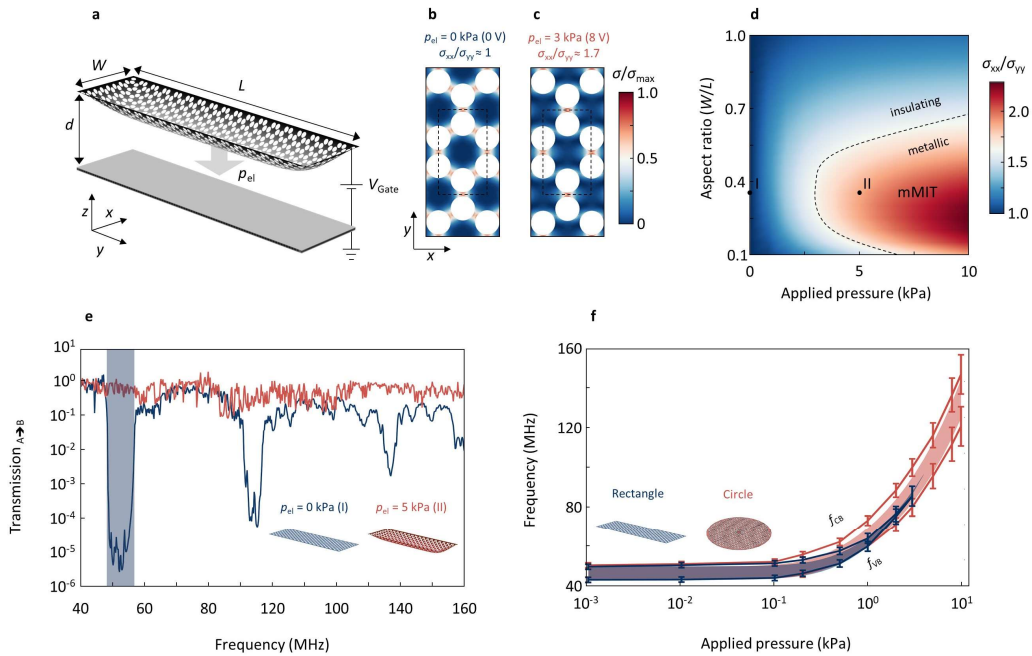


Figure 3 | Uniaxial tension engineering in a finite-size phononic system. **a**, Sketch of a finite-size system phononic device, which is mechanically deformed under electrostatic pressure, p_{el} , generated by a gate electrode below the graphene. **b,c**, Spatial tension distribution in the centre of the device with and without applied pressure. The dashed lines indicate the unit

cell of the lattice. **d**, Mechanical phase diagram: Tension uniaxiality (σ_{xx}/σ_{yy}) vs. pressure vs. device aspect ratio (W/L). The dotted line corresponds to $\sigma_{xx}/\sigma_{yy} = 1.7$, the degree in uniaxiality needed to induce the mMIT. **e**, Transmission for a device with an aspect ratio of 0.32 for $p_{el} = 0$ kPa (blue) and 5 kPa (red). The initially pronounced bandgap vanishes with applied pressure. **f**, Extracted valence band maximum (f_{VB}) and conduction band minimum (f_{CB}) vs. applied pressure for a rectangular device (blue, shown in (e)) and a circular device (red) as reference for uniform scaling ($\sigma_{xx}/\sigma_{yy} \approx 1$). For the rectangular device the mMIT occurs at 3 kPa, whereas the circular device maintains a bandgap over the entire range of applied pressures. The error bars depict the reading error of the simulation results, and the shaded areas correspond to the phononic bandgap extracted from band structure calculations.

Fabrication related challenges

Having demonstrated large frequency tunability as well as a change from a mechanically insulating to a metallic phase in graphene PnCs, we now want to assess the fabrication challenges associated with 2D materials. We therefore investigate the effect on the phononic bandgap for the two most common forms of disorder in 2D materials: surface contamination and random tension variations.

Perhaps the most widespread sources of contamination are “islands” of residues on top of the graphene. To simulate these added pieces of mass, we choose Polydimethylsiloxan (PDMS) as a typical polymer often used for transfer of 2D materials, and randomly place the pieces on the graphene membrane (Fig. 4a). At a thickness of 18 nm and a diameter of 4 μm , each piece has the same weight as the entire clean resonator. Next, we focus on the bandgap region and plot transmission vs. frequency for various amounts of added mass (Fig. 4b). Even for three added pieces (red), we still observe weak signatures of the phononic bandgap and conclude that the combined mass density of graphene and contamination must be on the order of $\rho_{2D} \leq 4\rho_{\text{graphene}}$. Values below this threshold have been observed in some graphene resonators in literature.^{32,35} We also test the effect of a uniform film of PDMS on the phononic device and still find a clear bandgap (see Supplementary information).

The second potential threat for breaking the phononic order are random tension variations in the suspended membrane commonly observed in both patterned and unpatterned graphene membranes.³¹ To model this effect, we generate disorder based on a superposition of randomized plane waves (details in Supplementary information). We take into account variations down to $1/4$ of the lattice constant of the phononic pattern. Two generated spatial tension distributions for small and large disorder are shown in Fig. 4c. The disorder strength is parametrized by the standard deviation of the distribution, $\sqrt{\text{Var}(\sigma)}/\sigma_0$

(see insets). We now calculate the transmission through the phononic device as a function of disorder strength. As shown in Fig. 4d, we find a gradual smearing out of the bandgap with increasing disorder. Above an estimated critical value of $\sqrt{\text{Var}(\sigma)}/\sigma_0 \approx 0.4$, the bandgap is no longer clearly distinguishable. If we compare this threshold to experimental values derived from Raman spectroscopy,^{36–38} we find similar spreads in tension. We conclude that it is challenging but possible to fabricate sufficiently uniform suspended devices. If, however more uniform samples are needed, we propose using thin multilayers of graphene, for which we find a bandgap up to a thickness of ~ 200 layers (see Supplementary information). For multilayer devices, we need larger pressures to induce the mMIT, but commonly used SiO₂/Si (300 nm) substrates allow applying ~ 100 V gate voltage before dielectric breakdown occurs, which translates to ~ 50 kPa (sufficient to induce the mMIT on multilayer devices). Overall, fabricating a PnC from suspended graphene with a pronounced bandgap is feasible.

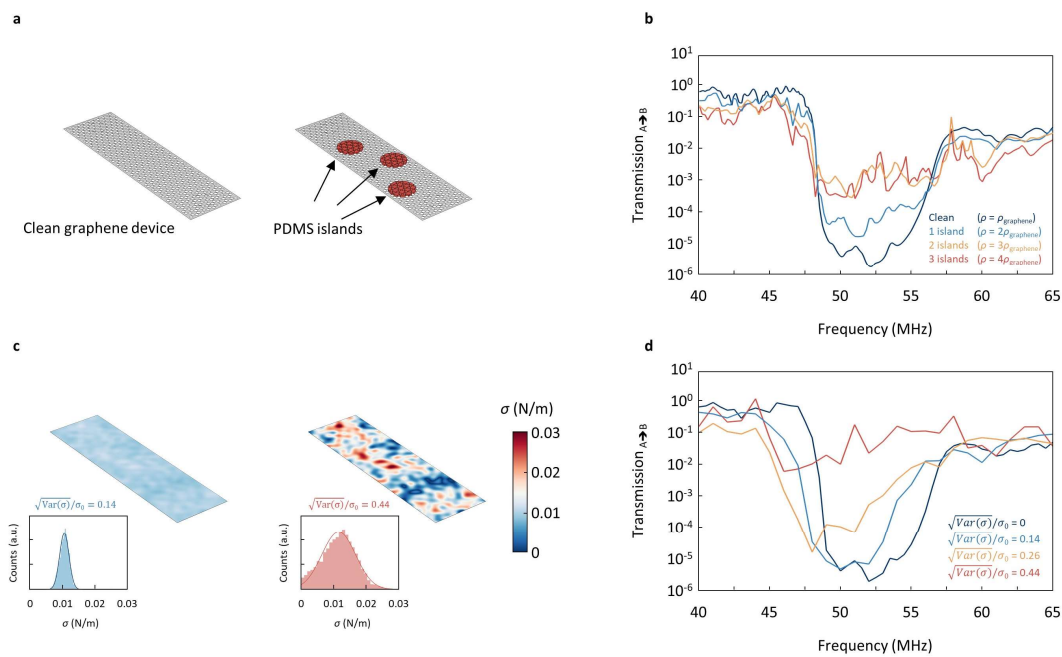


Figure 4 | The effect of disorder on the phononic bandgap. **a**, A phononic device with and without surface contamination. **b**, Phononic bandgap vs. added mass. With increasing degree of contamination, the bandgap smears out, yet remains visible up to areal mass density of $\rho_{2D} \approx 4\rho_{\text{graphene}}$. **c**, Graphene membrane before patterning with small and large tension disorder. The insets show the histograms used to extract the disorder strength: left, $\sqrt{\text{Var}(\sigma)}/\sigma_0 = 0.14$ and right, $\sqrt{\text{Var}(\sigma)}/\sigma_0 = 0.44$. **d**, Phononic bandgap vs. tension disorder. At a critical relative variation in tension $\sqrt{\text{Var}(\sigma)}/\sigma_0 \approx 0.40$ the bandgap vanishes.

Conclusion and outlook

We have demonstrated the manipulation of the phononic band structure by using uniaxial tension engineering and found closing of a phononic bandgap at $\sigma_{xx}/\sigma_{yy} = 1.7$. This corresponds to a transition from a mechanically insulating to a metallic (transmissive) phase. In a finite-size device, we can generate the required uniaxial tension distribution by applying a voltage of ~ 8 V to a gate electrode and observe vanishing of the phononic bandgap in transmission studies. This device can be considered a phononic counterpart to a field effect transistor, with acoustic transmission measurements taking the role of electrical transport. Furthermore, we discuss the feasibility of fabricating such a device with commonly used methods and extract a critical value for surface contamination ($\rho_{2D} \leq 4\rho_{\text{graphene}}$) and tension variations ($\sqrt{\text{Var}(\sigma)}/\sigma_0 \approx 0.40$).

The proposed system acts as a phononic transistor that can be used for phonon logic and invites realisation of a variety of logic gates as a next step. By varying the lattice constant a , the phononic system can be engineered to function in a broad range of frequencies from ~ 10 MHz to ~ 1 GHz. In addition, the proposed device design can serve as a switch controlling the coupling between two remote systems, e.g. mechanical resonators acting as qubits.^{19–21} This in principle also allows tunable dispersive readout of qubits via mechanical resonators. The proposed mMIT also makes it possible to control the phononic shielding of ultracoherent defect modes from the environment and therefore allows to dynamically study dissipation mechanisms. Finally, our demonstration of a phononic analogue to a mechanical metal-to-insulator transitions invite the consideration of analogues to other, more complex condensed matter physics phenomena, e.g. the quantum hall effect, Mott insulator transition, and topological phase transitions.

Methods

FEM Simulations

For the finite element modelling, we use COMSOL Multiphysics (Version 5.5) and assume the following material parameters for monolayer graphene: Young's modulus $E_{2D} = 1.0 \text{ TPa}^{28}$, Poisson's ratio of $\nu = 0.15$, thickness of $h = 0.335 \text{ nm}$ and a density of $\rho = \frac{\rho_{2D}}{h} = 2260 \text{ kg/m}^3$.

For details, see Supplementary information.

Acknowledgements

This work was supported by Deutsche Forschungsgemeinschaft (DFG, German Research Foundation, project-ID 449506295 and 328545488) and ERC Starting grant no. 639739.

References

1. Kushwaha, M. S., Halevi, P., Dobrzynski, L. & Djafari-Rouhani, B. Acoustic band structure of periodic elastic composites. *Phys. Rev. Lett.* **71**, 2022–2025 (1993).
2. Maldovan, M. Sound and heat revolutions in phononics. *Nature* **503**, 209–217 (2013).
3. Thomas, R. A. *et al.* Entanglement between distant macroscopic mechanical and spin systems. *Nat. Phys.* 1–6 (2020). doi:10.1038/s41567-020-1031-5
4. Riedinger, R. *et al.* Remote quantum entanglement between two micromechanical oscillators. *Nat. 2018 5567702* **556**, 473–477 (2018).
5. Mousavi, S. H., Khanikaev, A. B. & Wang, Z. Topologically protected elastic waves in phononic metamaterials. *Nat. Commun.* **6**, 1–7 (2015).
6. Pirie, H., Sadhuka, S., Wang, J., Andrei, R. & Hoffman, J. E. Topological Phononic Logic. *Phys. Rev. Lett.* **128**, (2022).
7. He, H. *et al.* Topological negative refraction of surface acoustic waves in a Weyl phononic crystal. *Nat. 2018 5607716* **560**, 61–64 (2018).
8. Tsaturyan, Y., Barg, A., Polzik, E. S. & Schliesser, A. Ultracoherent nanomechanical resonators via soft clamping and dissipation dilution. *Nat. Nanotechnol.* **12**, 776–783 (2017).
9. Ghadimi, A. H. *et al.* Elastic strain engineering for ultralow mechanical dissipation. *Science (80-.).* **360**, 764–768 (2018).
10. Yu, P. L. *et al.* A phononic bandgap shield for high-Q membrane microresonators. *Appl. Phys. Lett.* **104**, 23510 (2014).
11. Li, F., Liu, J. & Wu, Y. The investigation of point defect modes of phononic crystal for high Q resonance. *J. Appl. Phys.* **109**, 124907 (2011).
12. Wang, Y., Lee, J., Zheng, X. Q., Xie, Y. & Feng, P. X. L. Hexagonal Boron Nitride Phononic Crystal Waveguides. *ACS Photonics* **6**, 3225–3232 (2019).
13. Otsuka, P. H. *et al.* Broadband evolution of phononic-crystal-waveguide eigenstates in

- real- and k-spaces. *Sci. Rep.* **3**, 1–5 (2013).
14. Yang, L., Chen, J., Yang, N. & Li, B. Significant reduction of graphene thermal conductivity by phononic crystal structure. *Int. J. Heat Mass Transf.* **91**, 428–432 (2015).
 15. Gustafsson, M. V. *et al.* Propagating phonons coupled to an artificial atom. *Science (80-.).* **346**, 207–211 (2014).
 16. Kumar, S. *et al.* Temperature-Dependent Nonlinear Damping in Palladium Nanomechanical Resonators. *Nano Lett.* [acs.nanolett.1c00109](https://doi.org/10.1021/acs.nanolett.1c00109) (2021). doi:10.1021/acs.nanolett.1c00109
 17. Shin, H. *et al.* Control of coherent information via on-chip photonic-phononic emitter-receivers. *Nat. Commun.* **6**, 1–8 (2015).
 18. Zivari, A. *et al.* On-chip distribution of quantum information using traveling phonons. (2022).
 19. Navarathna, A. & Bowen, W. P. Good vibrations for quantum computing. *Nat. Phys.* **2022** 1–2 (2022). doi:10.1038/s41567-022-01613-z
 20. Luo, G. *et al.* Strong indirect coupling between graphene-based mechanical resonators via a phonon cavity. *Nat. Commun.* **9**, (2018).
 21. Cirac, J. I., Zoller, P., Kimble, H. J. & Mabuchi, H. Quantum State Transfer and Entanglement Distribution among Distant Nodes in a Quantum Network. *Phys. Rev. Lett.* **78**, 3221–3224 (1997).
 22. Hatanaka, D., Bachtold, A. & Yamaguchi, H. Electrostatically Induced Phononic Crystal. *Phys. Rev. Appl.* **11**, 1 (2019).
 23. Kirchhof, J. N. *et al.* Tunable Graphene Phononic Crystal. *Nano Lett.* **21**, 2174–2182 (2021).
 24. Zhang, Z.-D., Cheng, C., Yu, S.-Y., Lu, M.-H. & Chen, Y.-F. Electrically Tunable Elastic Topological Insulators Using Atomically Thin Two-Dimensional Materials Pinned on Patterned Substrates. *Phys. Rev. Appl.* **15**, 034015 (2021).
 25. Zhang, Q. H. *et al.* Graphene-Based Nanoelectromechanical Periodic Array with Tunable Frequency. *Nano Lett.* **21**, 8571–8578 (2021).

26. Novoselov, K. S. *et al.* Two-dimensional gas of massless Dirac fermions in graphene. *Nature* **438**, 197–200 (2005).
27. Castro Neto, A. H., Guinea, F., Peres, N. M. R., Novoselov, K. S. & Geim, A. K. The electronic properties of graphene. *Rev. Mod. Phys.* **81**, 109–162 (2009).
28. Lee, C., Wei, X., Kysar, J. W. & Hone, J. Measurement of the elastic properties and intrinsic strength of monolayer graphene. *Science (80-.)*. **321**, 385–388 (2008).
29. Deinhart, V. *et al.* The patterning toolbox FIB-o-mat: Exploiting the full potential of focused helium ions for nanofabrication. *Beilstein J. Nanotechnol.* **12**, 304–318 (2021).
30. Kovalchuk, S., Kirchhof, J. N., Bolotin, K. I. & Harats, M. G. Non-Uniform Strain Engineering of 2D Materials. *Israel Journal of Chemistry* (2022). doi:10.1002/ijch.202100115
31. Nicholl, R. J. T. *et al.* The effect of intrinsic crumpling on the mechanics of free-standing graphene. *Nat. Commun.* **6**, 8789 (2015).
32. Chen, C. *et al.* Performance of monolayer graphene nanomechanical resonators with electrical readout. *Nat. Nanotechnol.* **4**, 861–867 (2009).
33. Cha, J. & Daraio, C. Electrical tuning of elastic wave propagation in nanomechanical lattices at MHz frequencies. *Nat. Nanotechnol.* **13**, 1016–1020 (2018).
34. Kovalchuk, S. *et al.* Neutral and charged excitons interplay in non-uniformly strain-engineered WS₂. *2D Mater.* **7**, 35024 (2020).
35. Bunch, J. S. *et al.* Impermeable atomic membranes from graphene sheets. *Nano Lett.* **8**, 2458–2462 (2008).
36. Couto, N. J. G. *et al.* Random strain fluctuations as dominant disorder source for high-quality on-substrate graphene devices. *Phys. Rev. X* **4**, 1–13 (2014).
37. Neumann, C. *et al.* Raman spectroscopy as probe of nanometre-scale strain variations in graphene. *Nat. Commun.* **6**, 8429 (2015).
38. Colangelo, F. *et al.* Mapping the mechanical properties of a graphene drum at the nanoscale. *2D Mater.* **6**, (2019).

Supplementary information: Mechanical metal-insulator transition in 2D graphene phononic crystals

Jan N. Kirchhof^{1} and Kirill I. Bolotin^{1*}*

¹ Department of Physics, Freie Universität Berlin, Arnimallee 14, 14195 Berlin, Germany

[*jan.kirchhof@fu-berlin.de](mailto:jan.kirchhof@fu-berlin.de) [*kirill.bolotin@fu-berlin.de](mailto:kirill.bolotin@fu-berlin.de)

Finite element method simulations (FEM)

For all FEM-simulations presented in the main paper, we use the solid mechanics module of Comsol Multiphysics (Version 5.5).

Band structure calculations for an infinite lattice

The infinite model for the band structure calculations is based on two studies within the same model. In the first step we simulate the tension redistribution upon patterning (stationary study), which we use as input for a second study step in which we apply periodic boundary conditions to the unit cell and calculate the eigenfrequencies, which gives us the band structure. For all details see Ref. ¹. To assure that our simulations properly capture the phononic band gaps, we extend our calculations to more high symmetry points. For the unit cell shown in Fig. S1a, we plot the extended band structure for $\sigma_{xx}/\sigma_{yy} = 1$ and $\sigma_{xx}/\sigma_{yy} = 1.7$ inside the 1.Brillouin zone, Fig. S1b,c. We find that the valence band maximum between Γ and X and the conduction band minimum at X , and it is therefore sufficient to focus on the high symmetry points shown in the main paper.

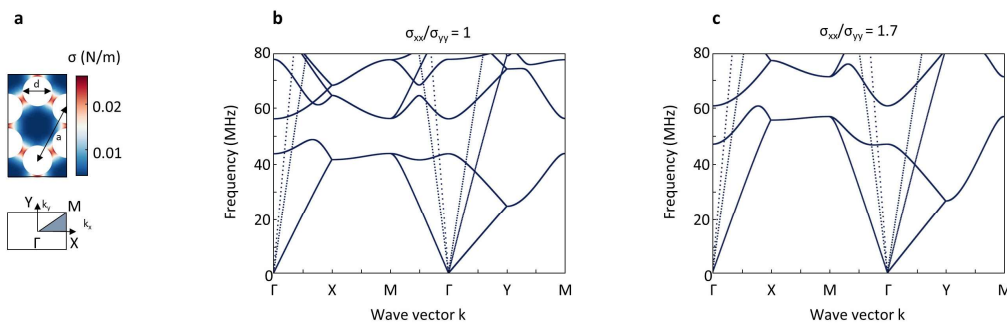


Figure S1 | Extended band structure. **a**, Unit cell of the honeycomb lattice with redistributed tension (top) and the corresponding first Brillouin zone (bottom). **b,c**, Extended phononic band structure for the unit cell shown in (a) with entirely uniform tension ($\sigma_{xx}/\sigma_{yy}=1$.) and implemented uniaxial tension $\sigma_{xx}/\sigma_{yy}=1.7$.

Transmission studies

To perform our transmission studies, we use a pre-stressed frequency domain study. In this study the phononic device is clamped along its perimeter (Fig. S2) and in a first study step we again calculate the tension redistribution upon patterning. In a second step, we add a time depended pressure in z direction at area A, which simulates an optothermal drive. For the transmission study, we then sweep the frequency of this time depended perturbation and calculate the response of the entire geometry (compare Eq. 1 main text). For this study step, we add isotropic damping ($\eta = 0.01$) to the graphene, which reproduces the quality factors ($Q \sim 100$) typically observed for graphene resonators at room temperatures. To simulate the effect of electrostatic pressure to the transmission studies, we add a boundary load to the entire device (including A and B) in z-direction and repeat the frequency sweep.

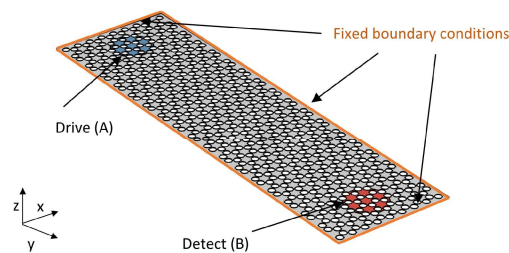


Figure S2 | Transmission geometry. The phononic device is clamped at its perimeter via fixed boundary conditions and motion is excited at A (blue) and detected at B (red).

Transmission circular reference device

As a comparison to the presented mMIT in the main text we perform transmission studies on a circular device under applied pressure which is excited at its centre and probed on the outside. The device geometry and resulting transmission spectra are shown in Fig. S3a,b, where we find clear band gap features (shaded area) with (red) and without (blue) applied pressure. In circular devices we find band gap features up to at least 30 kPa applied pressure in agreement with previous work.¹

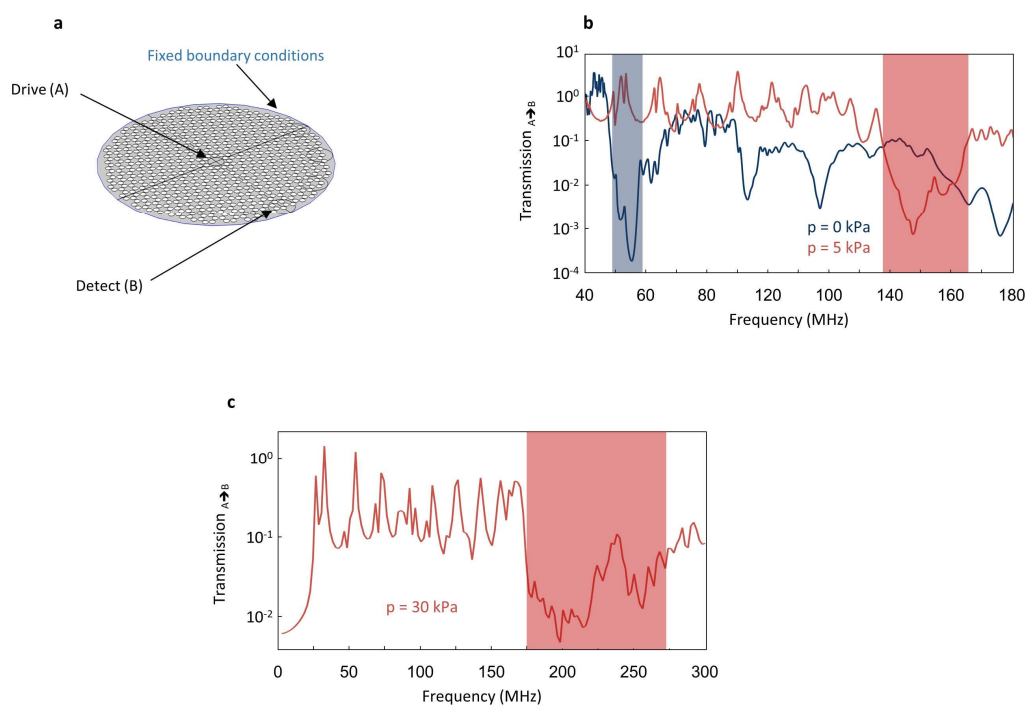


Figure S3 | Transmission circular reference device. a, Transmission geometry for a rectangular phononic device. At point A mechanical motion is excited by a frequency modulated laser, which then travels through the device and is detected at point B by a second laser spot. b,c Transmission from A to B vs. excitation frequency for the device shown in a) for 0, 5 and 30 kPa applied pressure. A clear bandgap region is visible for all cases.

Phononic bandgap vs. uniform residues

In addition to the added pieces of mass (Fig. 4 main text), we also investigate the effect of a uniform layer of resist, which could be present on a device after thermal annealing. In Fig. S4 we plot transmission for a device made from clean graphene (blue) and one contaminated with a 3 nm layer of PDMS (green). For both cases we find a clear bandgap, the added PDMS however causes a downshift in frequency as the entire device becomes heavier. Also the bandgap is slightly less pronounced, but still clearly noticeable. For PDMS we assume a Young's modulus of 0.75 MPa, a Poisson's ratio of 0.49 and a density of 970 kg/m³.

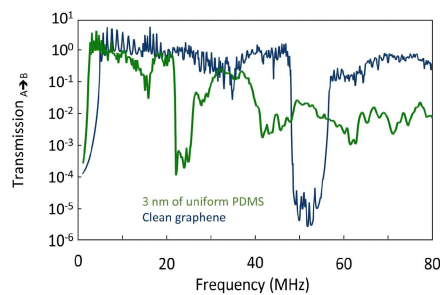


Figure S4 | Phononic bandgap vs. uniform residues. Transmission vs. frequency for a phononic device made from clean graphene (blue) and with a 3 nm uniform layer of PDMS residues (green).

Phononic bandgap vs. tension disorder

To represent a random but smooth enough spatial tension distribution in our devices we use a sum of plane waves with randomized amplitude $a(m, n)$ (between -1 and 1) and phase $\phi(m, n)$ (between 0 and π) of each mode:

$$\sigma(x, y) = p \sum_{m=-M}^M \sum_{n=-N}^N a(m, n) \cos(2\pi(mx + ny) + \phi(m, n))$$

The factor p controls the disorder strength.

Phononic band gap vs. layer number

As a potential approach to overcome challenges associated with the fabrication of uniform and residue free suspended graphene devices for phononic patterning, we suggest to use thin multilayers. For this we have to check, if the bandgap persist also for thicker devices. We thus perform band structure calculations for various thickness (maintaining a constant stress in the device) and extract the band gap (Fig. S5). We find a bandgap up to ~ 350 layers of graphene.

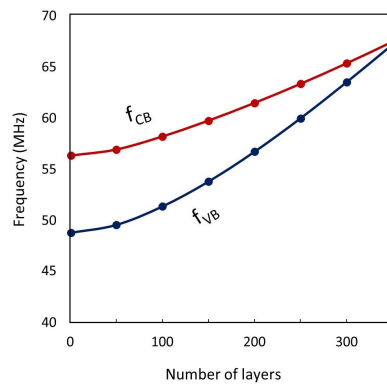


Figure S5 | Phononic band gap vs. layer number. Valence band maximum (f_{VB}) and conduction band minimum (f_{CB}) vs. number of graphene layers extracted from band structure calculations.

References

1. Kirchhof, J. N. *et al.* Tunable Graphene Phononic Crystal. *Nano Lett.* **21**, 2174–2182 (2021).